# Interstitial oxygen related defects and nanovoids in Au implanted *a*-$SiO_2$ glass depth profiled by positron annihilation spectroscopy



2015 J. Phys. D: Appl. Phys. 48 495302

(http://iopscience.iop.org/0022-3727/48/49/495302)

IOP Publishing Journal of Physics D: Applied Physics
J. Phys. D: Appl. Phys. **48** (2015) 495302 (11pp) doi:10.1088/0022-3727/48/49/495302

# Interstitial oxygen related defects and nanovoids in Au implanted *a*-$SiO_2$ glass depth profiled by positron annihilation spectroscopy

**L Ravelli[1], C Macchi[2,3], S Mariazzi[4], P Mazzoldi[5], W Egger[6], C Hugenschmidt[7], A Somoza[2,8] and R S Brusa[1]**

[1] Department of Physics, University of Trento and TIFPA-INFN, Via Sommarive 14, I-38123 Povo, Trento, Italy
[2] Instituto de Física de Materiales Tandil and CIFICEN (CONICET-UNCPBA), Pinto 399, B7000GHG Tandil, Argentina
[3] Consejo Nacional de Investigaciones Científicas y Técnicas (CONICET), Godoy Cruz 2290, (C1425FQB) CABA, Argentina
[4] Stefan-Meyer-Institut für subatomare Physik, Boltzmanngasse 3, 1090 Vienna, Austria
[5] Dipartimento di Fisica, Università di Padova, Via Marzolo 8, 35131 Padova, Italy
[6] Institut für Angewandte Physik und Messtechnik, Universität der Bunderswehr München, 85577 Neubiberg, Germany
[7] Physik Department E21 and FRMII, Technische Universität München, 85747 Garching, Germany
[8] Comisión de Investigaciones Científicas de la Provincia de Buenos Aires (CICPBA), Calle 526 entre 10y 11, (1900) La Plata, Argentina

E-mail: luca.ravelli@unitn.it

Received 18 August 2015, revised 29 September 2015
Accepted for publication 14 October 2015
Published 12 November 2015

**Abstract**

Samples of amorphous silica were implanted with Au ions at an energy of 190 keV and fluences of $1 \times 10^{14}$ ions $cm^{-2}$and $5 \times 10^{14}$ ions $cm^{-2}$ at room temperature. The damage produced by ion implantation and its evolution with the thermal treatment at 800 °C for one hour in nitrogen atmosphere was depth profiled using three positron annihilation techniques: Doppler broadening spectroscopy, positron annihilation lifetime spectroscopy and coincidence Doppler broadening spectroscopy. Around the ion projected range of $R_p = 67$ nm, a size reduction of the silica matrix intrinsic nanovoids points out a local densification of the material. Oxygen related defects were found to be present at depths four times the ion projected range, showing a high mobility of oxygen molecules from the densified and stressed region towards the bulk. The 800 °C thermal treatment leads to a recovery of the silica intrinsic nanovoids only in the deeper damaged region and the defect distribution, probed by positrons, shrinks around the ion projected range where the Au atoms aggregate. Open volume defects at the interface between Au and the amorphous matrix were evidenced in both the as implanted and in the thermal treated samples. A practically complete disappearance of the intrinsic nanovoids was observed around $R_p$ when the implantation fluence was increased by two orders of magnitude ($3 \times 10^{16}$ ions $cm^{-2}$). In this case, the oxygen defects move to a depth five times larger than $R_p$.

Keywords: glass, amorphous $SiO_2$, Au implantation, positrons, positronium, nanovoids

(Some figures may appear in colour only in the online journal)

 

## 1. Introduction

Amorphous silicon dioxide ( $a$-$SiO_2$), both in the form of silica glass and oxide thin films, is one of the key materials in many technological fields such as microelectronic, optoelectronic, optics and telecommunications [1, 2]. Intrinsic defects or introduced during manufacturing or device operation in harsh environments can have detrimental effects regarding optical and electronic properties [1–5]. Defects induced by ultraviolet (UV) irradiation are also responsible for the change of the refractive index in silica glass [6]. Defects in silica and their spectroscopic properties were deeply studied and reviewed in a number of books and papers [1–3, 7, 8]. The main defects, intrinsic or induced in silica, can be summarized as follows:

i) E' center: hole trapped at an oxygen vacancy $\equiv$ Si $\cdot$ $^{+}$ Si $\equiv$, where the point '$\cdot$' indicates an unpaired electron, '+' the trapped hole and the symbol '$\equiv$' three bonds to three oxygen atoms in the glass structure. This positively charged oxygen vacancy is a paramagnetic center that can be finely identified by electron spin resonance (EPR);
ii) Dangling oxygen bond $\equiv$ Si–O$\cdot$, named non bridging oxygen hole center (NBOHC). NBOHC were identified by EPR, photoluminescence (PL) and optical absorption (OA) in UV and vacuum ultraviolet (VUV);
iii) Peroxy radical (POR), $\equiv$ Si–O–O$\cdot$, that is also an active EPR center;
iv) Interstitial oxygen molecules $O_2$ residing in the interstitial space of $SiO_2$. A spectroscopic signature of an oxygen molecule is its infrared PL band at 1272 nm (0.975 eV). Interstitial O atoms can also exist as peroxyl $\equiv$ Si–O–O–Si $\equiv$ and ozonyl $\equiv$ Si–O–O–O–Si $\equiv$ linkages.

Both the structural modification and the formation of defects induced by irradiation of $a$-$SiO_2$ with electrons, neutrons, protons and photons was subject of many investigations with different analytical techniques such as electron paramagnetic resonance (EPR) [9], Raman scattering [10], infrared (IR) absorption [11, 12] and small-angle x-ray scattering (SAXS) [10].

Irradiation was also specifically employed to form defects with the aim of their study and identifications [13, 14]. Other effects occurring under irradiation are the structural disorder due to transformation from large to small ring structures [15] and the local densification of the silica glass, see [16] and references therein.

On the other hand, ion beam implantation of heavy metals (Au, Ag) was employed for the synthesis of metallic clusters in silica for tailoring the linear and non-linear optical response of the embedded nanostructures [17]. Noble metals nanoparticles are efficient scattering centers and/or absorbers of light in the visible or near infrared range. This property arises from the excitation of localized plasmon resonances at the surface of the metallic nanoparticles. Luminescence phenomena have been observed decreasing the size of the noble metal clusters down to sub-nanometer dimensions. These phenomena can be related to a transition regime between bulk and molecule-like structure properties of the ultra small clusters of which electronic configuration supports discrete electronic levels with an energy gap between the highest occupied and the lowest unoccupied molecular orbital (HOMO–LUMO gap) [18]. Room temperature photoluminescence (PL) emission of small Au nanoclusters of 5–10 atoms in size was reported in the 600–1500 nm wavelength range [19] and it was suggested that, in co-implanted Au and Er silica, part of the energy adsorbed by the Au nano-clusters is transferred to Er increasing the excitation cross section of the rare earth [20]. In these systems the presence of defects introduced by implantation near or at the surface of the nano-clusters and which are not completely recovered after the annealing treatments, can act as detrimental non-radiative recombination channels for the PL.

Aggregates of few atoms, which act as nucleation sites for the successive clustering process under thermal treatments, are already formed during implantation when the fluence exceeds the solubility threshold in the matrix [17]. Their size and depth dispersion depend on the ion fluence and the deposited energy. During thermal annealing, the aggregates first increase in size due to the atoms diffusing from the surrounding matrix, then by a coarsening process (Ostwald ripening) at the expense of the smaller aggregates. In the case of Au, due to its low diffusivity in silica [21], the distribution of the formed nanoclusters remains centred around the ion projected range.

Due to the non-uniform distribution of both the implanted species and the further formed nanoclusters, it is of peculiar interest to gain insight on the distribution of defects introduced by the implantation process and its evolution with thermal annealing. Although analytical techniques such as EPR and optical spectroscopies are extremely selective in identifying the type of defects in silica, they are not depth sensitive.

In this work, we have employed three complementary positron annihilation spectroscopy (PAS) techniques with the aim to depth profiling open volumes and oxygen related defects in silica samples implanted with Au. The implantation was performed at a low fluence (about $10^{14}$ Au $cm^{-2}$) at 190 keV, so that the size of the Au nanoclusters after thermal annealing of the samples is likely around 1 nm [22]. Annealing was done at a temperature of 800 °C, at which the original structure of the silica glass is usually considered to be completely recovered. As a first approach to the present work we reported some preliminary results as a case of the study obtained on a gold implanted silica glass sample using PAS [23]. As a result, our previous work was mainly addressed to point out the importance of PAS as an adequate not destructive technique to characterize open volume in disordered materials.

In silica-based materials, 60–80% of the implanted positrons form positronium (Ps) [24–26]. Ion or particle implantation in silica produce strong quenching of Ps because of the material compaction with a consequent reduction of the free volume available for Ps formation, oxygen enrichment of the trapping sites and competing trapping and annihilation of positrons at negatively charged oxygen-related defects. Quenching of Ps has evident effects on the observed positron lifetimes in silica and on the shape of the 511 keV positron annihilation line.

Doppler broadening spectroscopy (DBS) allowed to depth profile the overall damage. Positron annihilation lifetime spectroscopy (LS) was used to extract information on the defect type and the size variation of the intrinsic sub-nanovoids.

Coincidence doppler broadening spectroscopy (C–DBS) was applied to get the fraction of open volume defects decorating the Au atoms or aggregates formed after implantation and the Au nanoclusters after annealing.

The paper is organized as follows. In section 2 information on the implantation parameter and the thermal treatment of the samples is followed by a description of the three PAS techniques used to characterize and depth profile the damage. In section 3 we report the results obtained with LS, DBS and C–DBS and their discussion; in section 4 we give the conclusions of the present work.

## 2. Experimental

### 2.1. Samples

Samples were obtained from silica glass slabs (Herasil–1 by Heraeus) produced by fusion of natural quartz crystals. The slabs were implanted at room temperature with a 200 kV high-current implanter (Danfysik 1090) at the INFN Ion Implantation Laboratory (Legnaro, Italy). $Au^+$ ions at 190 keV were implanted in silica slabs with a fluence of $1 \times 10^{14}$ ions cm$^{-2}$ and $5 \times 10^{14}$ ions cm$^{-2}$. To avoid sample heating during implantation the ion flux was maintained at 0.1 $\mu$A cm$^{-2}$. The ion projected range $R_p$, i.e. the mean depth of the implanted Au distribution, was calculated by using SRIM program [27] and amounts to $R_p = 67$ nm with a straggling $\Delta R_p = 14$ nm. Samples implanted at $1 \times 10^{14}$ ions cm$^{-2}$ and $5 \times 10^{14}$ ions cm$^{-2}$ were annealed in nitrogen atmosphere at 800 °C for one hour. In the following the as-implanted samples with fluences of $1 \times 10^{14}$ ions cm$^{-2}$ and $5 \times 10^{14}$ ions cm$^{-2}$ will be identified as 1E14 and 5E14, and the two annealed samples as 1E14-A and 5E14-A, respectively. A further sample (3E16) was implanted in the same experimental condition of samples 1E14 and 5E14 but with a fluence of $3 \times 10^{16}$ ions cm$^{-2}$.

### 2.2. Lifetime spectroscopy (LS)

Positron lifetime measurements were performed with the pulsed monoenergetic positron beam of variable energy PLEPS (Pulsed Low Energy Positron System) [28, 29] at the high intensity positron source NEPOMUC (NEutron induced POsitron source MUniCh) [30, 31]. The measured lifetime spectrum consists of a sum of exponentials convoluted with the resolution function *R(t)* superimposed on a constant background *B*:

$$F(t) = R(t) \otimes \sum_{i=1}^{N} \frac{I_i}{\tau i} \exp\left(-\frac{t}{\tau_i}\right) + B \qquad (1)$$

where $\tau_i$ and $I_i$ are the positron lifetimes in the state $i$ and its relative intensities, respectively.

The positron lifetime is a measure of the electron density at the annihilation site [24–26], therefore, positron lifetime values increase when positrons become trapped in open volumes with increasing size. In many materials, when the open volume reaches the sub-nanometer size, Ps can be formed [24–26]. Positronium is formed in two states: a singlet state, para-positronium (p-Ps) (total spin 0 and formation probability 1/4) and a triplet state, ortho-positronium (o-Ps) (total spin 1 and formation probability 3/4). In vacuum, p-Ps annihilates into two gamma rays of 511 keV with a lifetime of 125 ps, whereas o-Ps annihilates into three gamma rays with a lifetime of 142 ns. The lifetime of o-Ps formed in open voids is reduced by the $2\gamma$ pick-off process in which the positron annihilates with an electron of opposite spin of the medium. The size of the nano or sub-nanovoids is directly linked to the reduced lifetime of the o-Ps.

Positron lifetime spectra were acquired in a range of positron implantation energy of 0.5–18 keV. The overall (detector plus pulsing system) time resolution was 280 ps. At each energy 3–5 $\times 10^6$ were acquired with a counting rate of 8000 counts per second.

The mean positron implantation depth $\bar{z}$ in nanometers is related to the positron implantation energy $E$ by the equation $\bar{z} = (40/\rho)E^{1.6}$ when the material density $\rho$ (2.2 g cm$^{-3}$ for fused silica glass) and energy $E$ are expressed in g cm$^{-3}$ and keV, respectively [24–26].

The analysis to extract the lifetime and intensity values from the measured spectra was performed with the POSFIT program [32]. A good fit to the data was obtained by deconvolving the spectra into three lifetime components.

### 2.3. Doppler broadening spectroscopy (DBS)

The depth distribution of the damage was obtained by the analysis of the DBS measurements [25, 26]. With depth profiling DBS technique the 511 keV positron-electron annihilation line $G(E, E_\gamma)$ where $E_\gamma$ is the energy of the detected gamma quanta, is measured at different positron implantation energies $E$. The recorded annihilation line in the laboratory frame is Doppler broadened by the motion of the electron-positron annihilating pair. The longitudinal momentum component $p_L$ of the electron-positron pair with respect to the detector direction is related to the energy shift $\Delta E = |E_\gamma - 511\ \text{keV}|$, where $E_\gamma$ is the energy of the detected gamma quanta, by the equation: $p_L = \frac{2\Delta E}{c}$. Therefore, the shape of $G(E, E_\gamma)$ gives the one-dimensional momentum distribution of the annihilation radiation convoluted with the resolution function. The low-momentum part of the spectrum is mainly due to positron annihilation with valence electrons and it is characterized by the so-called shape parameter $S$ defined as the ratio between the counts in a central area and the counts in the total area of the annihilation peak. The high-momentum part arises from annihilations with core or outmost core electrons which are a fingerprint of the chemical nature of the atom [33–35]. The detailed study of the core annihilation region gives information on the atoms surrounding the positron annihilation site but, because these annihilation events are very rare, a coincidence measurement is necessary to suppress the background (see paragraph 2.4).

DBS measurements were performed with a continuous positron beam at the Trento University [36, 37] coupled with a high purity germanium detector [HPGe] 45% efficiency, 1.4 keV resolution at 511 keV. The $S$ parameter was acquired with

a microspectra method and stabilized by a software procedure [38]. To calculate the $S$ parameter, the energy windows were chosen as: $|511 - E_\gamma| \leqslant 0.85$ keV and $|511 - E_\gamma| \leqslant 4.25$ keV for the central and the total area of $G(E, E_\gamma)$ respectively. The $S$ parameters were measured with a statistical error of 0.1% (more than $2.5 \times 10^5$ counts in each annihilation spectrum) and normalized to the $S$ value of bulk Si ($S^b_{\mathrm{Si}} = 0.537$): $S_n = S/S^b_{\mathrm{Si}}$. This choice allows the comparison with data on silica samples obtained in other laboratories [25].

### 2.4. Coincidence broadening spectroscopy (C–DBS)

The signal from positron-core electron annihilation can be used to obtain information on the chemical species surrounding the annihilation site [33–35]. Since positrons are repelled by the ion core, the annihilation probability with core electrons is low. To extract information from the high momentum region of the spectrum, the background must be reduced by a coincidence technique with two germanium detectors. The coincidence measurements were done at the high intensity positron source NEPOMUC [31, 39, 40] with a resolution in coincidence of 1.1 keV at 511 keV, acquiring about $2 \times 10^7$ counts for each spectrum. To highlight the fingerprint signal coming from the atom around the annihilation site, data are presented as a ratio curve of the measured spectrum with respect to the measured spectrum obtained measuring a reference sample. As a reference, in this work we have used a coincidence spectrum measured in the bulk of a Si single-crystal. A spectrum $G_{\mathrm{Au}}(25\ \mathrm{keV}, E_\gamma)$ in Au single crystal was also measured in order to obtain the characteristic feature of this element in the high momentum annihilation region. The fingerprint of positron annihilation in bulk silica glass was obtained by measuring the coincidence spectrum $G_{\mathrm{glass}}(25\ \mathrm{keV}, E_\gamma)$.

## 3. Results and discussion

At first, the distribution and evolution of the defects as a function of depth is discussed. An analysis of the type and fraction of defects at the surface of the Au nanoclusters will follow.

### 3.1. Depth profiling of the damage

The depth profile of the damage due to implantation and its evolution with thermal annealing can be extracted by analysing the $S_n$ versus $E$ curves measured with DBS technique. The $S_n$ versus $E$ curves for 1E14 and 1E14-A samples are shown in figure 1 while those for 5E14 and 5E14-A samples in figure 2.

The data were modelled using the positron stationary diffusion equation. Dashed lines through the experimental points are the best fit to the data obtained by this model. The $S_n$ versus $E$ data for the virgin silica glass (Herasil-1) together with its fitting line are also shown in figure 1. For clarity, only the fitting curve for Herasil-1 is shown as a continuous line in figure 2.

The $S_n$ values in the Herasil samples monotonically increase from a characteristic value $S_s$ (∼0.965) to a value $S_b$ (∼0.99) due to positron annihilation in the surface and bulk

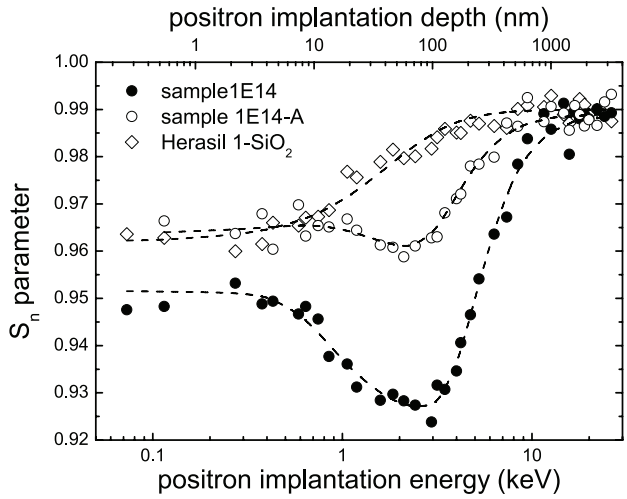


**Figure 1.** Line shape parameter $S_n$ as a function of the positron implantation energy (lower axis) for Herasil 1 silica glass, Au implanted sample at a fluence of $1 \times 10^{14}$ ions cm$^{-2}$ (1E14) and the irradiated sample annealed at 800 °C for one hour (1E14-A). Dashed lines through the experimental points are the best fit obtained with the positron diffusion equation. The mean positron implantation depth $\bar{z}$ is indicated on the upper axis. Experimental errors are within the symbols.

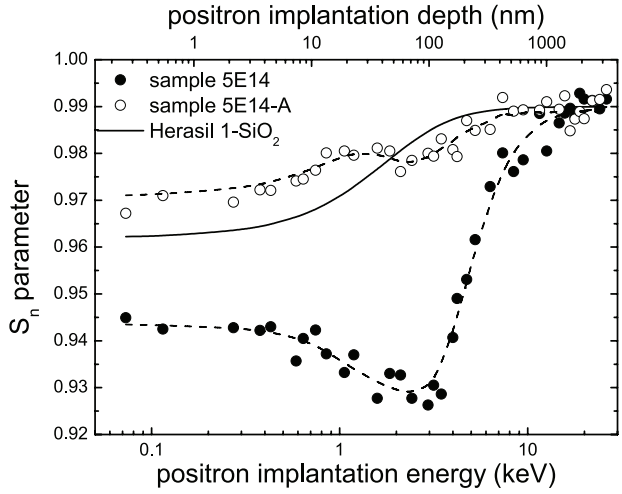


**Figure 2.** Line shape parameter $S_n$ as a function of the positron implantation energy (lower axis) for the Au implanted sample at a fluence of $5 \times 10^{14}$ ions cm$^{-2}$ (5E14) and the irradiated sample annealed at 800 °C for one hour (5E14-A). Dashed lines through the experimental points are the best fit with the positron diffusion equation. Only the fitting line for Herasil-1 silica glass is shown for clarity (experimental points in figure 1). The mean positron implantation depth $\bar{z}$ is indicated on the upper axis. Experimental errors are within the symbols.

states, respectively. At each positron implantation energy, the $S_n(E)$ values can be expressed as a linear combination of $S_s$ and $S_b$:

$$S_n(E) = S_b f_b(E) + S_s f_s(E) \tag{2}$$

where $f_b(E)$ and $f_s(E)$ are the fractions of positron annihilating in the bulk and surface states, respectively.

The produced ion implantation damage is evidenced by a strong decrease in the $S_n$ parameter values. The experimental

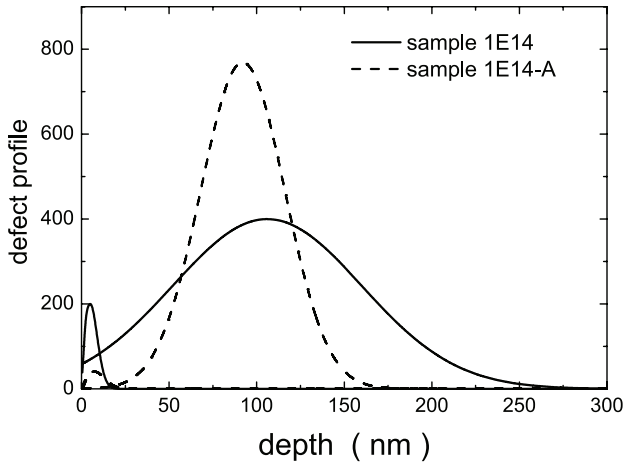


**Figure 3.** Defect profiles as obtained by the fitting of the $S_n$ versus $E$ curves of figure 1 with the positron stationary diffusion equation. Solid line: sample implanted at a fluence of $1 \times 10^{14}$ ions cm$^{-2}$ (1E14); Dashed line: sample annealed at 800 °C for one hour (1E14-A).

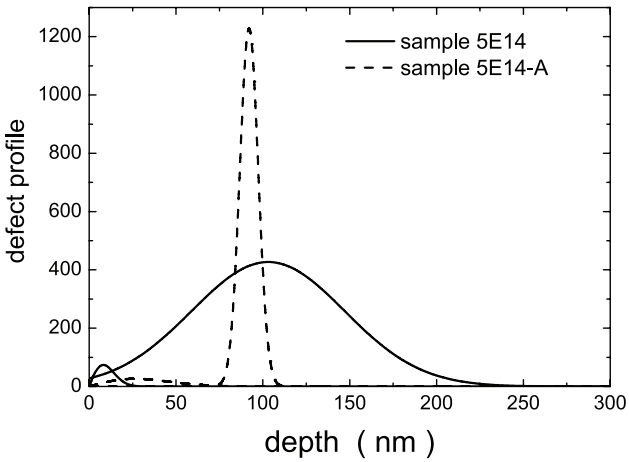


**Figure 4.** Defect profiles as obtained by the fitting of the $S_n$ versus $E$ curves of figure 2 with the positron stationary diffusion equation. Solid line: samples implanted at fluence of $5 \times 10^{14}$ ions cm$^{-2}$ (5E14); Dashed line: sample annealed at 800 °C for one hour (5E14-A).

data show a well pronounced minimum around (2–3) keV positron implantation energy, see figures 1 and 2. The shape of the $S_n$ versus $E$ curve and the $S_n$ value of ~0.925 at the minimum, are similar in both implanted samples. The observed broadening of the 511 keV annihilation line (i.e. decrease of $S_n$ values) is attributed to an increase of positron annihilations with oxygen electrons and by Ps quenching [24–26]. p-Ps annihilations contribute to the central region of the Doppler broadened line, their decrease in the quenching process is reflected in a lowering of the $S_n$ values.

The thermal annealing at 800 °C gives rise to a partial recovery of the damage. In the 1E14-A sample, the $S_n$ surface values match to those of Herasil-1 before implantation and the minimum in the curve rises to about $S_n = 0.96$. On the contrary, the minimum in sample 5E14-A is less evident, and a small increase of the $S_n$ values above the Herasil curve around 1 keV positron implantation energy is observed.

The $S(E)$ values in the implanted and thermally treated samples can be described by a linear combination which takes into account positron trapping into defects:

$$S(E) = S_b f_b(E) + S_s f_s(E) + \sum_i S_{di} f_{di}(E) \tag{3}$$

where $S_{di}$ and $f_{di}(E)$ are the characteristic $S$ parameter of the defect of type $i$ and the fraction of positron annihilation in the defect $i$, respectively.

The $S(E)$ curves were modelled, as in [37, 38, 41], with the positron diffusion equation to extract the distribution of the defect profile. The probability $f_b(E)$, $f_s(E)$ and $f_{di}(E)$, are related to the stationary density $n(z, E)$ of thermal positrons at depth $z$ by the equations:

$$\begin{aligned} f_b &= \lambda_b \int_0^\infty n(z,E)\,\mathrm{d}z \\ f_s &= D_+ \left[\frac{\mathrm{d}n(z,E)}{\mathrm{d}z}\right]_{z=0} \\ f_{di} &= \nu_i \int_0^\infty C_i(z) n(z,E)\,\mathrm{d}z \end{aligned} \tag{4}$$

where $\lambda_b$ is the bulk positron annihilation rate (taken as the inverse of the mean lifetime in the bulk $\lambda_b = 1/\langle\tau_b\rangle = 1/1060\,\mathrm{ps}^{-1}$), $D_+$ the positron diffusion constant, $\nu_i$ the specific trapping rate per unit defect concentration, $C_i(z)$ the defect profile. The positron density $n(z, E)$ is the solution of the positron diffusion equation:

$$D_+ \frac{\partial n(z,E)}{\partial z} - \left[\lambda_b + \sum_i \nu_i C_i(z)\right] n(z,E) + P(z,E) = 0 \tag{5}$$

The positron implantation profile $P(z, E)$ [24, 25, 33] is given as input while the functional forms of the defect profiles $C_i(z)$ are inserted as a guess and $\nu_i$ is a fitting parameter.

The positron diffusion length in the virgin sample was found to be $L_+ = \sqrt{D_+\tau_b} = 48$ nm. Two defect profiles were needed to obtain a good fit to the implanted and thermal treated samples: a derivative of a Gaussian and a Gaussian for the first and the second distribution were adopted, respectively. The defect profiles $C(z)$ are shown in figures 3 and 4. The integral of $C(z)$ is proportional to the number of traps [37, 38, 41].

In both samples, implanted and annealed, there is a first defect distribution very near to the surface and a second one which extends very deeply in the sample. The $S_n$ values characterizing the defects were found to be $S_{d1} \cong 0.92$ and $S_{d2} \cong 0.95$, for the two defect distributions, respectively. In the implanted samples, the first distribution is confined in a region of 40 nm from the surface ($E < 2$ keV) and the corresponding number of near surface traps is about thirty times lower than the traps in the second distribution. After annealing the number of traps becomes ninety and fifteen times lower than in the second distribution.

The majority of the traps are in the second distribution which reaches a depth of about four times the $R_p$ value of the as implanted samples. The maximum of the Gaussian distribution is around 100 nm depth in both samples. An extension of the defected layer beyond the $R_p$ position, was also observed by positron techniques in silica implanted with $Ar^+$ at 30 keV

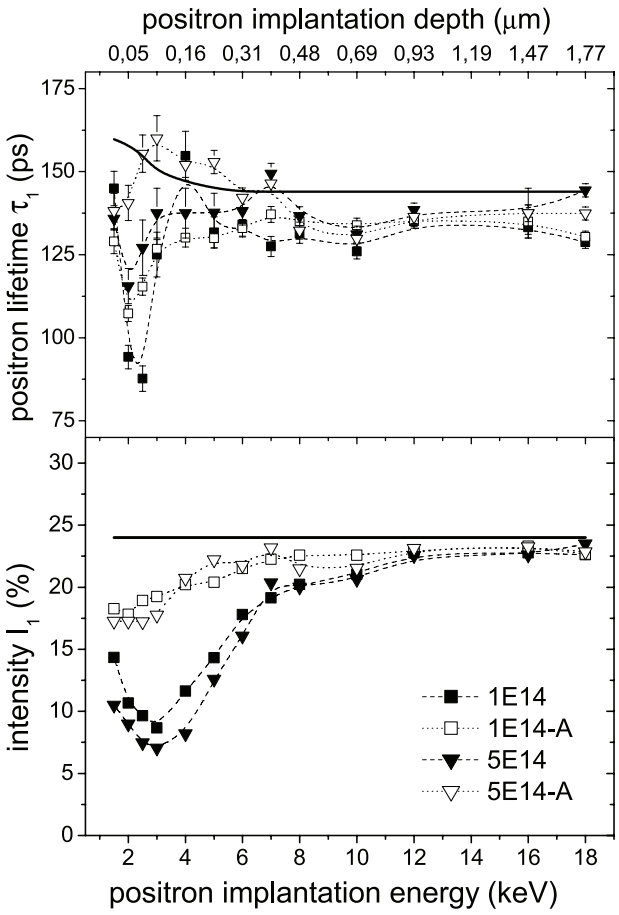


**Figure 5.** Lifetime $\tau_1$ and its associated intensity $I_1$, as a function of the positron implantation energy (lower axis) for the Herasil-1 silica glass (solid line), implanted samples at fluence of $1 \times 10^{14}$ ions cm$^{-2}$ (1E14) and $5 \times 10^{14}$ ions cm$^{-2}$ (5E14). Results on the samples annealed at 800 °C for one hour (1E14-A, 5E14-A) are also shown. The mean positron implantation depth $\bar{z}$ is indicated on the upper axis. The dashed lines are guides to the eye.

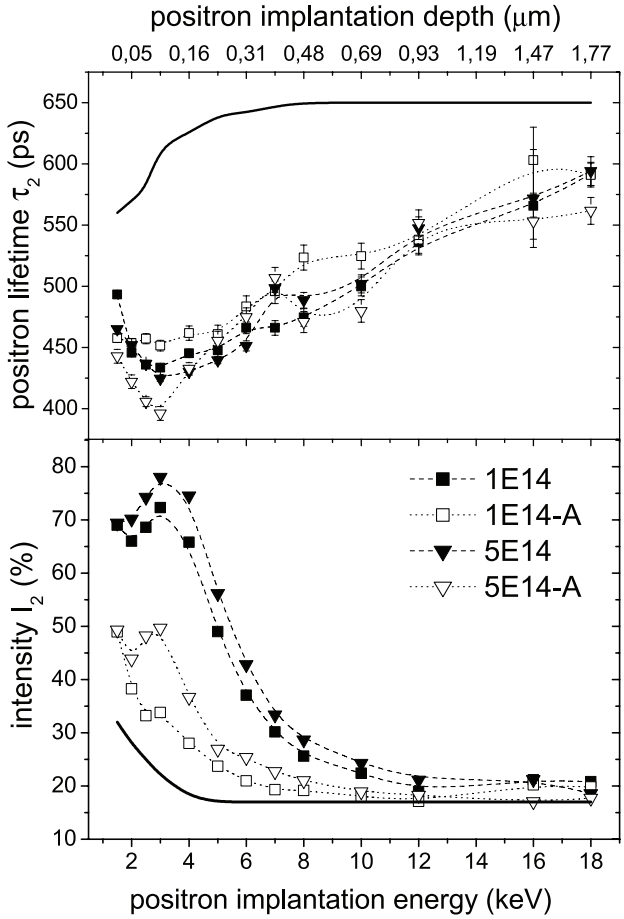


**Figure 6.** Lifetime $\tau_2$ and its associated intensity $I_2$, as a function of the positron implantation energy (lower axis) for the Herasil-1 silica glass (solid line), implanted samples at fluence of $1 \times 10^{14}$ ions cm$^{-2}$ (1E14) and $5 \times 10^{14}$ ions cm$^{-2}$ (5E14). Results on the samples annealed at 800 °C for one hour (1E14-A, 5E14-A) are also shown. The mean positron implantation depth $\bar{z}$ is indicated on the upper axis. The dashed lines are guides to the eye.

and 50 keV energy at a fluence of $1 \times 10^{17}$ Ar$^+$ cm$^{-2}$ [42]. In that case the damage extended only two times the ion projected range.

After annealing the centre of the Gaussian moves, in both samples, to ∼90 nm depth but the distribution squeezes more significantly in the 5E14-A sample: the FWHM reduces at about ∼50 nm and only ∼15 nm in the 1E14-A and 5E14-A samples, respectively.

### *3.2. Oxygen related defects and size variation of sub-nanovoids*

The lifetime spectra of all samples and of bulk silica were well decomposed into three lifetime components. The variance of the fit was always in the 1.0–1.2 range. The lifetimes and their respective intensities obtained for the implanted and annealed samples are plotted and compared in figure 5 (lifetime $\tau_1$, intensity $I_1$), figure 6 (lifetime $\tau_2$, intensity $I_2$) and figure 7 (lifetime $\tau_3$, intensity $I_3$). The data are shown as a function of the positron implantation energy $E$ (lower axis) and the mean positron implantation depth $\bar{z}$ (upper axis). In the figures, the lifetimes and the associated intensities corresponding to the Herasil-1 silica bulk are plotted as a solid line. The damaged region, as obtained by DBS measurements, extends from the surface to about 250 nm depth for the as implanted samples. This depth corresponds to a mean positron implantation depth at an implantation energy of ∼5 keV. After annealing, the damaged region is confined in the first 180 nm ($E \cong 4.2$ keV) for the sample 1E14-A, and in the first 120 nm ($E \cong 3.4$ keV) for the sample 5E14-A.

We will discuss at first the positron lifetimes characterizing the Herasil-1 silica glass. Above 4 keV positron implantation energy, the lifetime and intensity values are characteristic of the Hearasil-1 silica glass bulk. For positron implantation energies lower than 4 keV, an increasing fraction of positrons and Ps annihilates in a surface state.

The longest lifetime in the Herasil-1 bulk ($\tau_3 \approx 1600$ ps, $I_3 \approx 57\%$) comes from pick-off annihilation of Ps formed in the intrinsic sub-nanovoids of the silica glass:

$$\frac{1}{\tau_3} = \frac{1}{\tau_{\text{pick-off}}} + \frac{1}{\tau_T} \tag{6}$$

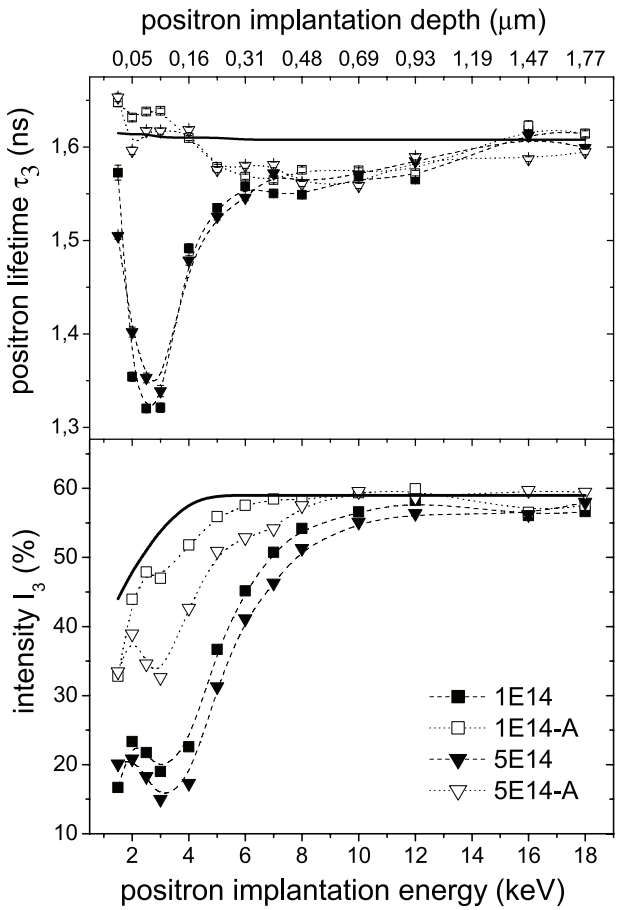


**Figure 7.** Lifetime $\tau_3$ and its associated intensity $I_3$, as a function of the positron implantation energy (lower axis) for the Herasil-1 silica glass (solid line), implanted samples at fluence of $1 \times 10^{14}$ ions cm$^{-2}$ (1E14) and $5 \times 10^{14}$ ions cm$^{-2}$ (5E14). Results on the samples annealed at 800 °C for one hour (1E14-A, 5E14-A) are also shown. The mean positron implantation depth $\bar{z}$ is indicated on the upper axis. The dashed lines are guides to the eye.

where $\tau_T = 142$ ns is the o-Ps lifetime in vacuum and $\tau_{\text{pick-off}}$ is the pick-off lifetime . The $\tau_{\text{pick-off}}$ is correlated with the average size of the nano-voids, in which o-Ps annihilates, by the Tao-Eldrup semiempirical model [43–45]. This model is very accurate to estimate size voids below 2 nm in silica-based materials [46]. Variations in the radius of the voids of 0.01 nm can be easily detected [47, 48].

In the Tao-Eldrup model the void hosting Ps is assumed to be spherical with an effective radius $R$. Such a Ps trap is considered as an infinite potential well with its radius increased to $R + \Delta R$, ($\Delta R = 0.166$ nm) being an empirical parameter which describes the penetration of Ps wave function into the bulk [45]. The relationship between $\tau_{\text{pick-off}}$ (in ns) and the radius $R$ (in nm) is the following:

$$\tau_{\text{pick-off}} = 0.5\left[\frac{\Delta R}{R+\Delta R} + \frac{1}{2\pi}\sin\left(2\pi\frac{R}{R+\Delta R}\right)\right]^{-1} \text{ns} \qquad (7)$$

In Herasil-1 the o-Ps pick-off lifetime results in $(1.640 \pm 0.011)$ ns. The corresponding radius of the intrinsic sub-nanovoids is $(0.250 \pm 0.001)$ nm. In this silica sample about 77% of implanted positrons are found to form Ps in sub-nanovoids (4/3 $I_3$).

The second lifetime ($\tau_2 \approx 650$ ps, $I_2 \approx 17\%$) is attributed to annihilation of trapped positrons and Ps that is quickly quenched in smaller voids. It is worth to note that both trapped positrons and positron of Ps undergoing pick-off, annihilate with the oxygen atoms decorating the walls of the sub-nano-voids. Annihilations of free positrons and p-Ps contribute to the shortest lifetime ($\tau_1 \approx 150$ ps, $I_1 \approx 24\%$).

Near the surface, less o-Ps formation ($I_3 \approx 36\%$ with respect to 58% into the bulk) is balanced by more positrons annihilating at surface trapped states increasing the intensity $I_2$ from 17% to 40%.

In implanted Herasil-1 strong variation of the lifetimes and intensities values are observed as a consequence of the introduced oxygen related defects and variation in the size of the intrinsic nanovoids.

The variation of $\tau_1$ and $\tau_2$ in implanted silica glass and crystalline quartz were correlated with the type of defects discussed in [49]. In that experiment samples were irradiated with different doses of fast neutrons and then studied using PAS techniques and ESR as a function of isochronal annealings up to a temperature of 1200 °C. The $\tau_1$ lifetime increasing from about 150 ps to about 200 ps was associated to the presence of NBOHC defects, whereas the decrease of $\tau_2$ from (700–600) ps to (400–500) ps was associated to the detection of oxygen molecules in interstitial positions. Positrons appeared to be insensitive to E' and POR defects, as also confirmed by photo blenching experiments.

In Herasil-1 after Au implantation and subsequent annealing, very pronounced changes of lifetimes and intensities were observed in the first 250 nm ($E < 5$ keV). The monotonous increase of the lifetimes and their intensities from positron implantation energies of (4–5) keV (160–250 nm) to 10 keV, see figures 5–7, is due to positrons probing both the bulk and the defected region during their diffusion motion. Towards the surface of the samples, below 50 nm, the increase of all the three lifetimes points out a less defected structure. This region corresponds to the first defect profile obtained by the analysis of DBS data.

In the as implanted samples, around $E = 3$ keV, depth ~100 nm (see figure 7), the intensity $I_3$ associated with the positron fraction forming o-Ps and annihilating via pick-off decreases and reaches a minimum value of ~20% in the 1E14 sample and of ~15% in the 5E14 sample. A slight maximum at 2 keV (~50 nm) is observed before the minimum. The o-Ps lifetime $\tau_3$ also decreases from ~1600 ps to ~1300 ps in both samples indicating that in this region there is a reduction of free volumes for Ps formation. Here, the mean radius of the voids becomes $R = (0.215 \pm 0.001)$ nm. Both, the decrease of o-Ps formation and its lifetime are due to a reduction of free volume available for Ps formation because of compacting and/or enrichment of free volume by displaced oxygen created in the Frenkel process. These measurements show that the major compaction of the material is just around $R_p + \Delta R_p$. In the simple approximation that the free volume fraction can be expressed as $f_v = C I_3 \langle v_h \rangle$ [50], where $\langle v_h \rangle$ is the mean volume of the nanovoids and $C$ a constant related to the o-Ps formation, the free volume in this region reduces to 20% of the free volume in the Herasil-1.

After implantation the intensity $I_1$ due to p-Ps and free positron annihilations (figure 5) is reduced from ∼24% to ∼(7–9)%. The non-observed increase of $\tau_1$, seems to exclude a sizable presence of NBOHC defects.

Defects with unpaired electrons and displaced oxygen atoms or molecules are competitive traps for positrons. Their presence is revealed by the decrease of $\tau_2$ from about 600 ps to ∼425 ps in both samples 1E14 and 5E14. Around 3 keV, intensity $I_2$ increases at a maximum of about 80% where $I_3$ reaches its minimum. This behaviour indicates that the majority of positrons after implantation annihilate with oxygen and negatively charged oxygen-related defects.

Positrons also probe, as will be shown in section 3.3, the presence of Au atoms. The positron lifetime in pure defect free Au is 100 ps and in Au vacancy clusters spans from 200 to 400 ps. But, due to the atomic size of the Au aggregates in the present samples, positrons would be mainly trapped in open volumes at the Au–$SiO_2$ interfaces annihilating with both Au and O electrons. These annihilations can be expected to give a slight contribution to $\tau_1$, $I_1$ and $\tau_2$, $I_2$.

The presence of damage in implanted silica was observed to extend beyond $R_p$ by etching and leaching the samples [51, 52]. In contrast to these techniques, PAS depth profiling probes directly and non destructively the in depth modification of the silica matrix. At depth distant from the most damaged region around $R_p$, the decrease of the Ps formation and consequently the diminution of the free volumes can be ascribed to the filling of the $SiO_2$ rings with interstitial oxygen.

Using first-principle schemes based on density-functional theory, stable configurations of oxygen introduced into the $SiO_2$ rings were found to be the peroxyl and ozonyl linkages which consist of two or three oxygen atoms bonded together and with two silicon atoms, and the oxygen molecule $O_2$ [53, 54]. The $O_2$ interstitial configuration is energetically favoured with respect to the ozonyl and peroxyl linkages, respectively. The formation energy of $O_2$ residing in a ring, calculated referred to an isolate $O_2$ and the unperturbed oxide, was shown to depend on the size of the interstitial volume and to be below 1 eV from ∼80 Å$^3$ up to 250 Å$^3$ [54].

Different studies [53–55] on oxygen diffusion in silica glass and quartz crystals suggest that the interstitial $O_2$ molecule is the main diffusion species since the activation energy for the diffusion process is less than 1 eV [55]. The interstitial oxygen do not strongly interact with the $SiO_2$ matrix and diffuse much faster than lattice oxygen. It was also reported that $O_2$ can diffuse being inserted within Si–O–Si bond with an activation energy of 0.7 eV [53].

Compaction of the implanted layer, as probed by the reduction of free volume available for Ps formation, is expected to induce a tensile stress gradient from the ion stopping region towards the underlying layers of the sample. An increased diffusion of the interstitial oxygen along this stress gradient may account for the observed in depth defect distribution. For previous experimental evidences of in depth damage in implanted silica see discussion in [42] and references therein. PAS depth profiling measurements in $Ar^+$ implanted silica [42] have shown that the damage distant from the $R_p + \Delta R_p$ region, like in the present Au implanted silica samples, is strongly related to the presence of oxygen defects. In the present Au implanted samples, oxygen defects are found two times more deeper than in $Ar^+$ implanted samples. Injection of defects due to stress relaxation was also observed by PAS in Si substrate of deposited thin carbon films [56].

Thermal treatment induces a partial recovery of the glass structure in the damaged region, more evident in the 1E14-A than in the 5E14-A sample (see figures 5–7 and DBS data in figures 1 and 2).

The o-Ps lifetime $\tau_3$ returns to values around 1600 ps like in the Herasil-1 glass, showing a partial reconstruction of the silica structure. Conversely, in the region of the minimum, $\tau_2$ increases and slightly decreases in the 1E14-A and 5E14-A sample, respectively. Anyway, its lifetime values range around 450 ps. This points out that oxygen defects are still present after annealing at 800 °C. This lifetime stays well below the typical value in the Herasil-1 glass (about 600 ps). For the 1E14-A sample, the intensities $I_2$ and $I_3$ approach the intensity values of the Herasil-1. For the 5E14-A sample at energies slightly lower than 3 keV, a minimum in the $I_3$ curve (35%) and a maximum in the $I_2$ curve (50%) are always well visible at the position of the maximum of the defect distribution reported in figure 4. Here, due to the shrinking of the defect distribution, the defect concentration is higher for the sample 5E14-A than that of 1E14-A. On the contrary, for the sample 1E14-A the distribution of defects is broader and the defect concentration is lower. As a consequence, in the region around the maximum of the defects distribution the structure of the intensities $I_2$ and $I_3$ are hardly visible.

The increase of the intensity $I_1$ follows the variation of $I_3$ values mainly due to p-Ps annihilations.

### 3.3. Defects near Au particles

C-DBS coincidence spectra in the implanted and thermal annealed silica glass were measured at 2 keV implantation energy, corresponding to a positron mean implantation depth near the ion projected range $R_p$.

The CDB spectra are presented as a function of electron momentum $p_L$ in the form of difference of momentum distribution relative to the Si spectrum $G_{Si}(E_\gamma)$ divided by the same spectrum $G_{Si}(E_\gamma)$:

$$G_i^0 = \frac{G_i(E_\gamma) - G_{Si}(E_\gamma)}{G_{Si}(E_\gamma)} \tag{8}$$

Following the procedure described in [34] to obtain the relative difference ratio curves, all experimental data points were treated using a smoothing routine from $15 \times 10^{-3}\ m_0c$ till $60 \times 10^{-3}\ m_0c$ which consists on averaging n channels increasing from 3 to 7 in the selected $p_L$ range. Furthermore, the smoothed spectra were normalized to a total area of one in the whole momentum range.

In figure 8 the ratio curve of Au and Herasil-1 silica glass, as obtained with equation (8), are shown. The ratio curve of Au has two peaks centred at $\sim 12 \times 10^{-3}\ m_0c$ and $35 \times 10^{-3}\ m_0c$. Herasil-1 curve has a first peak at $10 \times 10^{-3}\ m_0c$ followed by a bump with a maximum around $40 \times 10^{-3}\ m_0c$, which is in

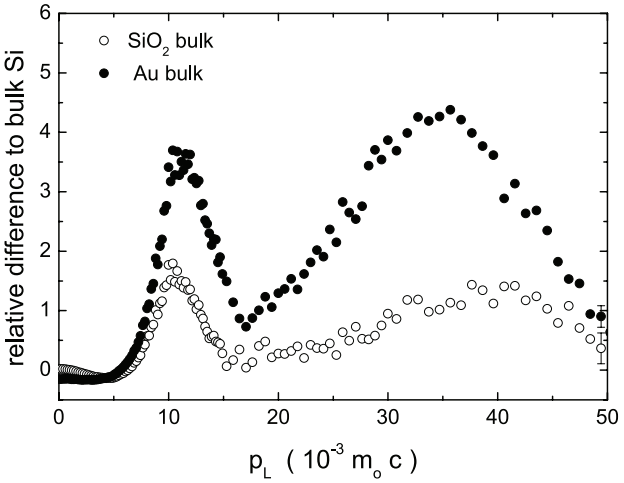


**Figure 8.** C–DBS ratio curves of Au and Herasil-1 silica glass with respect to a Si reference sample. The maximum errors are shown on the last points in the figure.

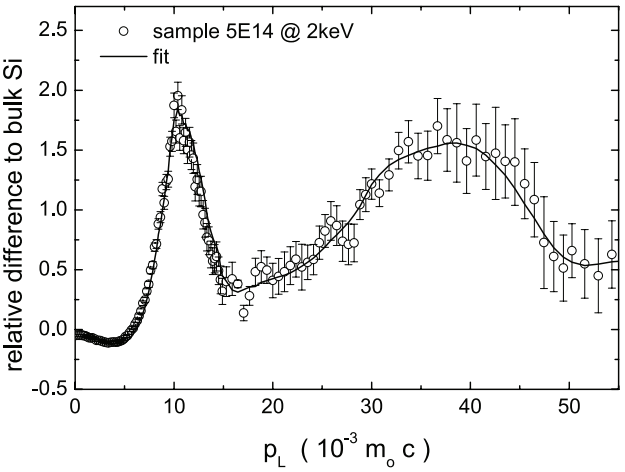


**Figure 9.** C-DBS ratio curve of sample implanted at a fluence of $5 \times 10^{14}$ ions cm$^{-2}$. The solid line is the fit obtained with equation (9).

**Table 1.** Fraction $f_{Au}$ of positrons annihilating with Au electrons.

| Samples | | | CDB @ 2 keV |
|---|---|---|---|
| Sample | Dose | Thermal treatment | $f_{Au}$ |
| 1E14 | $1 \times 10^{14}$ | — | $21 \pm 1$ |
| 1E14-A | $1 \times 10^{14}$ | Annealed 1 h 800 °C | $16 \pm 1$ |
| 5E14 | $5 \times 10^{14}$ | — | $14 \pm 1$ |
| 5E14-A | $5 \times 10^{14}$ | Annealed 1 h 800 °C | $2 \pm 1$ |

*Note*: The fractions were obtained by fitting the ratio curve of the implanted and annealed samples.

agreement with previous studies on both amorphous silica and crystalline quartz [57].

The ratio curve of sample 5E14 is indicated in figure 9. Similar curves were obtained for the other three samples studied in this work. To have a rough estimation of the fraction of positrons annihilating in proximity to Au particles, these curve were fitted with a linear combination of the Au and $SiO_2$ curves of figure 8:

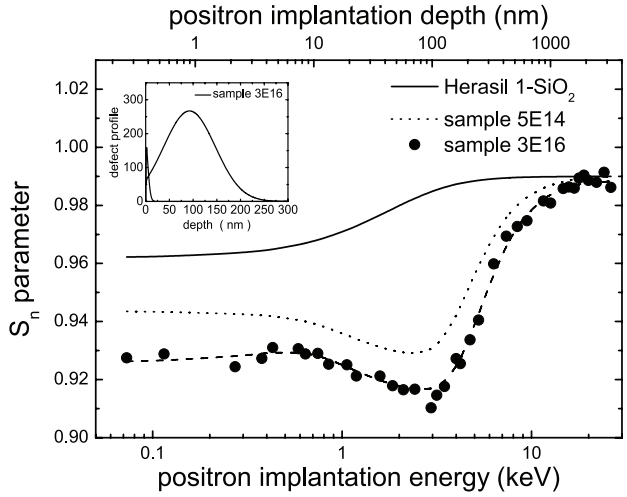


**Figure 10.** Line shape parameter $S_n$ as a function of the positron implantation energy (lower axis) for samples implanted with Au ions at fluence of $3 \times 10^{16}$ ions cm$^{-2}$. The dashed lines through the experimental points are the best fit with the positron diffusion equation. For comparison, the fitting on the experimental data measured in Herasil-1 and 5E14 sample are shown as well (in solid and dotted lines, respectively). The defect profiles obtained by the fitting procedure on the 3E16 sample are shown in the inset. The mean positron implantation depth $\bar{z}$ is indicated on the upper axis. Experimental errors are within the symbols.

$$G_0 = f G^0_{Au} + (1 - f) G^0_{SiO_2} \tag{9}$$

where $f$ is the fraction of positron annihilating with Au high momentum electrons. This fitting procedure can be justified by the fact that the $SiO_2$ curve is a fingerprint of positron annihilation with oxygen atoms and, in a first approximation, can be also assumed for positron annihilation at oxygen related defects or positron of Ps annihilating by pick-off into nanovoids.

The fractions $f$ as obtained by the fitting procedure are summarized in table 1.

The positron fraction annihilating in proximity to the Au particles reduces with the annealing and with increasing the irradiation dose. Both these effects can be explained by the diffusion of Au atoms towards the $R_p$ region and their clustering [17]. Clustering was indirectly evidenced by the shrinking of the defect distribution near $R_p$ (see figures 3 and 4) which is the region where the disorder of the matrix and the defects concentrate after annealing. Clustering reduces the number of Au sites and, as a consequence, the Au–$SiO_2$ interface area in which positrons can be trapped. This effect is more marked when more Au atoms, i.e. in the sample irradiated with the highest dose, are present in the matrix.

### *3.4. Compaction by increasing the Au implantation fluence*

In this section we show that increasing the Au fluence of two order of magnitude the positron lifetime signals saturate due to the high sensitivity of PAS.

An additional sample was implanted with Au ions at an energy of 190 keV in the same experimental condition of

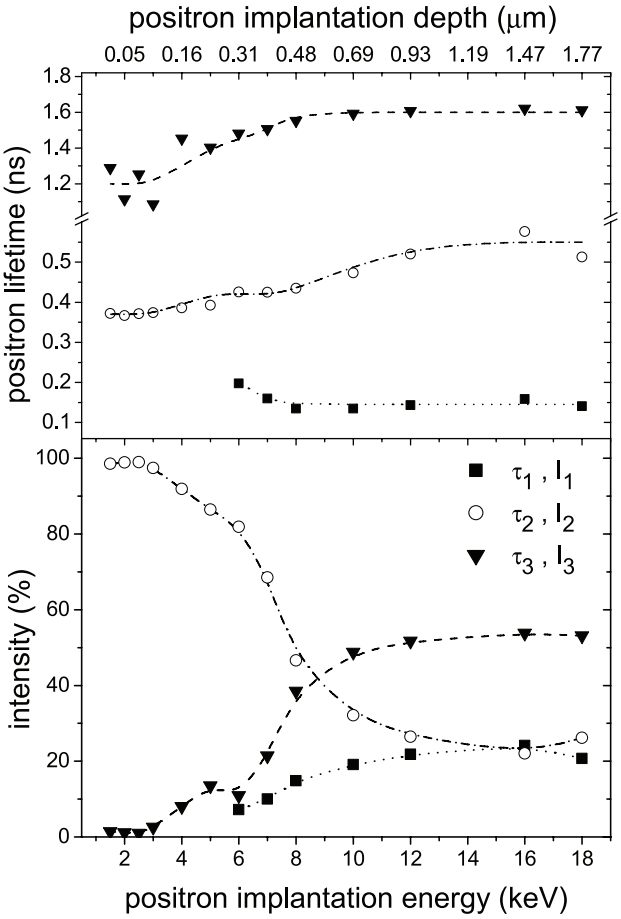


**Figure 11.** Lifetimes and their corresponding intensities, as a function of the positron implantation energy (lower axis) for implanted sample at a fluence of $3 \times 10^{16}$ ions cm$^{-2}$. The mean positron implantation depth $\bar{z}$ is indicated on the upper axis. The dashed lines are guides to the eye.

samples 1E14 and 5E14, but with a much higher fluence of $3 \times 10^{16}$ ions cm$^{-2}$ (sample 3E16).

In figure 10 the DBS measurements are presented and the defect profiles extracted by the diffusion model are shown in the inset. For comparison the $S_n$ versus $E$ curves of Herasil-1 and of the 5E14 sample are also shown as solid and dotted lines, respectively.

From the fitting procedure, the $S_n$ values characterizing the defects, $S_{d1}$ and $S_{d2}$, were found to have the same values than that of the samples implanted at a lower fluence. This result indicates that the type of defects does not change with the fluence. The defects produced by Au implantation range deeper down to a depth of 330 nm from the surface, about five times the implantation projected range (see inset in figure 10). This depth is 25% larger than that found in the sample implanted at a fluence of $10^{14}$ ions cm$^{-2}$. The deep damage reflects the higher stress field due to the high Au dose that promotes the clustering of Au atoms already during the implantation.

In the defected region around $R_p$, the shortest lifetime disappears while $\tau_2$ and $\tau_3$ slightly decrease below 400 ps and 1600 ps, respectively (see figure 11). The intensity $I_2$ reaches nearly the value of 100% and the intensity $I_3$ reduces to a few percent. This behaviour shows that increasing the fluence up to $10^{16}$ ions cm$^{-2}$ leads to a strong decrease of the silica intrinsic nanovoids with a heavy local densification of the material.

## 4. Conclusions

In this work, we have used different positron annihilation spectroscopy techniques to analyse the depth profiles of interstitial oxygen related defects and nanovoids in Au implanted amorphous silica. For this aim, firstly $a$–$SiO_2$ was implanted at room temperature with Au at an energy of 190 keV and two different fluences. Then, the implanted samples were annealed for one hour in nitrogen atmosphere at 800 °C. The damage produced by ion implantation and its evolution with the thermal treatment is discussed in terms of a local densification of the silica matrix around the ion projected range $R_p$ where the Au atoms aggregate. The obtained results reveal that interstitial oxygen related defects were found at depths four times greater than $R_p$ which indicates a high mobility of oxygen molecules from the densified and stressed region towards the $a$–$SiO_2$ glass bulk. It was also found that the size of the silica intrinsic nanovoids recover to the original size only in the deeper damaged region after annealing. However, open volume defects at the Au/$SiO_2$ interface are still present in both the as implanted and the thermally treated samples. When the fluence was increased by two orders of magnitude, the intrinsic nanovoids around $R_p$ almost complete vanish and oxygen defects move to a depth five times larger than $R_p$.

We have also shown that the non-destructive PAS techniques are able to depth profile damage generated in a disordered system by implantation of heavy ions. The most striking features are the possibility (i) to probe with positrons, as a function of depth, the local densification of silica looking at the shrinking or disappearance of intrinsic nanovoids. As a matter of fact, densification of silica glass induced by high hydrostatic pressure and high irradiation doses of neutrons, ions, protons, gamma rays, or electrons, was extensively studied. The main drawback in those cases is that homogenous densified thick layers were considered; (ii) to detect open volume defects at the interface of the metal aggregates and the silica matrix which could influence the optical response of the glass; and (iii) to accurately determine the depth range of the highly mobile interstitial oxygen molecules diffusing in silica. The last two points are significant issues when investigating the influence of defects in changing photoluminescence properties in the visible and near-infrared ranges of silica for applications in several applied fields as sensing, photovoltaics, catalysis and nonlinear optics.

Future works with PAS techniques could be carried out on even more complex amorphous silica systems under co-implantation of noble metals and rare earths with the aim to correlate open volume defects evolution, and the consequent introduction of different electronic states, with changes in the optical response of the silica-based materials.

## Acknowledgments

The Forschungs-Neutronenquelle Heinz Maier-Leibnitz (FRMII) facility is gratefully acknowledged for allocation of beam time at the NEPOMUC facility. This work was partially supported by Agencia Nacional de Promoción Científica y Tecnológica (PICT 2011-1088), Consejo Nacional de Investigaciones Científicas y Técnicas (Argentina) (PIP # 112-201101-00793), Comisión de Investigaciones Científicas de la Provincia de Buenos Aires (Res. # 833/014) and SECAT–UNCPBA (Argentina).

## References

[1] Pacchioni G, Skuja L and Grisom D L (ed) 2000 *Defects in $SiO_2$ and Related Dielectrics: Science and Technology* (Dordrecht: Kluwer)
[2] Devine R A B, Duraud J P and Dooryhée E (ed) 2000 *Structure and Imperfections in Amorphous and Crystalline Silicon Dioxide* (New York: Wiley)
[3] Awazu K and Kawazoe H 2003 *J. Appl. Phys.* **94** 6243
[4] Griscom D L 2011 *J. Non-Cryst. Solids* **357** 1945
[5] Girard S, Kuhnhenn J, Gusarov A, Brichard B, Uffelen M V, Ouerdane Y, Boukenter A and Marcandelia C 2013 *IEEE Trans. Nucl. Sci.* **60** 2015
[6] Donadio D, Bernasconi M and Boero M 2001 *Phys. Rev. Lett.* **87** 195504
[7] Griscom D L 1991 *J. Ceram. Soc. Japan* **99** 923
[8] Skuja L, KaJihara K, Hirano M and Hosomo H 2012 *Nucl. Instrum. Meth.* B **286** 159
[9] Hosono H, Kawazoe H and Matsunami N 1998 *Phys. Rev. Lett.* **80** 317
[10] Bates J B, Hendricks R W and Schaffer L B 1974 *J. Chem. Phys.* **61** 4163
[11] Mazzoldi P, Carnera F, Caccavale F, Favaro M L, Boscolo-Boscoletto A, Granozzi G, Bertoncello R and Battaglin G 1991 *J. Appl. Phys.* **70** 3528
[12] Kajihara K, Hirano M, Skuja L and Hosono H 2008 *Phys. Rev.* B **78** 094201
[13] Skuja L, Güttler B, Schiel D and Silin A R 1998 *Phys. Rev.* B **58** 14296
[14] Magruder R H, Weeks R A and Weller R A 2011 *J. Non-Cryst. Solids* **357** 1615
[15] Yang T, Gao Y, Huang X, Zhang Y, Toulemonde M, Xue J, Yan S and Wang Y 2011 *J. Non-Cryst. Solids* **357** 3245
[16] Buscarino G, Agnello S, Gelardi F M and Boscaino R 2009 *Phys. Rev.* B **80** 094202
[17] Mattei G, Mazzoldi P and Bernas H 2010 *Metal Nanoclusters for Optical Properties* ed H Barnes (Berlin: Springer) p 287
[18] Link S, Beeby A, FitzGerard S, El-Sayed M A, Schaaff T and Whetten R L 2002 *J. Phys. Chem.* B **106** 3410
[19] Cesca T, Maurizio C, Kalinic B, Scian C, Trave E, Battaglin G, Mazzoldi P and Mattei G 2014 *Nucl. Instrum. Meth.* B **326** 7
[20] Cesca T, Kalinic B, Maurizio C, Scian C, Battaglin G, Mazzoldi P and Mattei G 2014 *Nanoscale* **6** 1716
[21] Collins D, Schroeder D and Sah C T 1966 *Appl. Phys. Lett.* **8** 323
[22] Maurizio C, Perotto G, Trave E, Pellegrini G, Mattei G and Mazzoldi P 2010 *Nucl. Instrum. Meth.* B **268** 3219
[23] Brusa R S *et al* 2010 *Nucl. Instrum. Meth.* B **268** 3186–90
[24] Dupasquier A and Mills A P Jr (ed) 1995 *Positron Spectroscopy of Solids* (Amsterdam: North-Holland)
[25] Krause-Rehberg R and Leipner H S 1999 *Positron Annihilation in Semiconductors* (*Defect Studies, Springer Series in Solid State Science*) (Berlin: Springer)
[26] Asoka-Kumar P, Lynn K G and Welch D O 1994 *J. Appl. Phys.* **76** 4935
[27] Biersack J P and Haggmark L 1980 *Nucl. Instrum. Meth.* B **174** 257 (SRIM code at www.srim.org)
[28] Egger W 2010 *Physics with Many Positrons* ed R S Brusa *et al* (Amsterdam: North-Holland) p 419
[29] Sperr P, Egger W, Kögel G, Dollinger G, Hugenschmidt C, Repper R and Piochacz C 2008 *Appl. Surf. Sci.* **255** 35
[30] Hugenschmidt C 2010 *Physics with Many Positrons* ed R S Brusa *et al* (Amsterdam: North-Holland) p 399
[31] Hugenschmidt C, Löwe B, Mayer J, Piochacz C, Pikart P, Repper R, Stadlbauer M and Schreckenbach K 2008 *Nucl. Instrum. Meth.* A **593** 616
[32] Kirkegaard P, Olsen J V, Eldrup M M and Pederson N J 2009 *PALSfit: A Computer Program for Analyzing Positron Lifetime Spectra* (Roskilde: Danmarks Tekniske Universitet)
[33] Asoka-Kumar P, Alatalo M, Ghosh V J, Kruseman A C, Nielsen B and Lynn K G 1996 *Phys. Rev. Lett.* **77** 2097
[34] Brusa R S, Deng W, Karwasz G P and Zecca A 2002 *Nucl. Instrum. Meth.* B **194** 519
[35] Alatalo M, Barbiellini B, Hakala M, Kauppinen H, Korhonen T, Puska M J, Saarinen K, Hautojärvi P and Nieminen R M 1996 *Phys. Rev.* B **54** 2397
[36] Zecca A, Bettonte M, Paridaens J, Karwasz G P and Brusa R 1998 *Meas. Sci. Technol.* **9** 409
[37] Macchi C, Mariazzi S, Karwasz G P, Brusa R S, Folegati P, Frabboni S and Ottaviani G 2006 *Phys. Rev.* B **74** 174120
[38] Brusa R S, Karwasz G P, Tiengo N, Zecca A, Corni F, Tonini R and Ottaviani G 2000 *Phys. Rev.* B **61** 10154
[39] Stadlbauer M, Hugenschmidt C and Schreckenbach K 2008 *Appl. Surf. Sci* **255** 136
[40] Hugenschmidt C *et al* 2008 *Appl. Surf. Sci.* **255** 29
[41] Brusa R S, DuarteNaia M, Zecca A, Nobili C, Ottaviani G, Tonini R and Dupasquier A 1994 *Phys. Rev.* B **49** 7271
[42] Mazzoldi P, Mattei G, Ravelli L, Egger W, Mariazzi S and Brusa R S 2009 *J. Phys. D: Appl. Phys.* **42** 115418
[43] Eldrup M 1982 *Positron Annihilation* ed Coleman P G *et al* (Amsterdam: North-Holland) pp 753–72
[44] Tao S J 1972 *J. Chem. Phys.* **56** 5499
[45] Eldrup M, Lightbody D and Sherwood N J 1981 *Chem. Phys.* **63** 51
[46] Gidley D W, Frieze W E, Dull T L, Yee A F, Ryan E T and Ho H M 1999 *Phys. Rev.* B **60** 5157(R)
[47] Zanatta M, Baldi G, Brusa R S, Egger W, Fontana A, Gilioli E, Mariazzi S, Monaco G, Ravelli L and Sacchetti F 2014 *Phys. Rev. Lett.* **112** 045501
[48] Sasaki Y, Nagay Y, Ohkubo H, Inoue K, Tang Z and Hasegawa M 2003 *Radiat. Phys. Chem.* **68** 569
[49] Hasegawa M, Saneyasu M, Tabata M, Tang Z, Nagai Y, Chiba T and Ito Y 2000 *Nucl. Instrum. Meth.* B **166–167** 431
[50] Jean Y C 1990 *Microchem. J.* **42** 72
[51] Arnold G W, Marchi G D, Mazzoldi P and Battaglin G 1996 *Nucl. Instrum. Meth.* B **116** 364
[52] Battaglin G, Arnold G W, Mattei G, Mazzoldi P and Dran J C 1999 *J. Appl. Phys.* **85** 8040
[53] Chelikowsky J R, Chadi D J and Binggeli N 2000 *Phys. Rev.* B **62** 2251(R)
[54] Bongiorno A and Pasquarello A 2004 *Phys. Rev.* B **70** 195312
[55] Kajihara K, Kamioka H, Hirano M, Miura T, Skuja L and Hosono H 2005 *J. Appl. Phys.* **98** 013529
[56] Brusa R S, Macchi C, Mariazzi S, Karwasz G, Laidani N, Bartali R and Anderle M 2005 *Appl. Phys. Lett.* **86** 221906
[57] Hugenschmidt C, Pikart P and Schreckenbach K 2009 *Phys. Status Solidi* C **6** 2459